ATLAS Detector Status

A. Henriques
CERN, Geneva, Switzerland

(representing the ATLAS collaboration)

Abstract

ATLAS is a general-purpose detector that will exploit the full potential of the LHC p-p collision programme. An attempt to describe the ATLAS detector concept and the recent developments are given.This is a very important phase of the project, with most of the Technical Design Reports of all the components already submitted.

1 Introduction

The ATLAS Collaboration proposes to build a general-purpose pp detector which is designed to exploit the full discovery potential of the Large Hadron Collider (LHC). LHC will provide 10 times higher centre-of-mass energy and 100 times higher proton-proton collision rates than previous colliders. This opens up a new frontier of physics. ATLAS will explore this great potential, which can be exemplified both within today's theoretical framework and using extrapolations and guesses of what might lie beyond it.

The Standard Model, which is the established theoretical description of the basic building blocks of matter and of the fundamental interactions, has several unexplored aspects, all well within the reach of ATLAS:

- The mass-generating mechanism or spontaneous symmetry breaking, which predicts the existence of a scalar particle, the Higgs boson.
- The decay modes of the top quark and the precise determination of its mass.
- The origin of matter/antimatter asymmetry, CP-violation, which is expected to be observable in many decays involving the bottom quark.

Theoretical developments indicate the possible existence of a more general framework for the building blocks of matter and the fundamental interactions, Supersymmetry. This leads to two important predictions:

- The existence of at least five different Higgs bosons, most often within the mass range accessible to ATLAS.
- A large spectrum of new particles produced at a mass scale that ATLAS will be able to establish and measure with high precision in most cases.

ATLAS at LHC will greatly increase the resolving power with which the size of the building blocks of matter, the quarks and leptons, can be measured. Good sensitivity to a possible substructure of the fundamental fermions will be achieved up to a scale of ~ 30 TeV.

The discovery of the Z and W particles was a large step forward in the understanding of fundamental interactions. ATLAS will be able to discover and measure particles with similar properties but with masses up to 50 times larger than those of the W and Z.

ATLAS is designed for a large discovery potential and for precision measurements. Experience and theoretical knowledge tell us that an experiment with this ambition should detect clean signals and perform accurate measurements of charged leptons, photons, non-interacting particles such as neutrinos through missing energy measurements, hadronic jets and bottom quarks. In addition ATLAS should provide reconstruction of complete final states, such as the decay products of B-hadrons at low luminosity.

The ATLAS detector will start operating in the year 2005 with a detector that is 22 m high, 44 m long and has an overall weight of about 7000 tons. The basic design concept to achieve its goals includes three detector systems illustrated in figure 1.1:

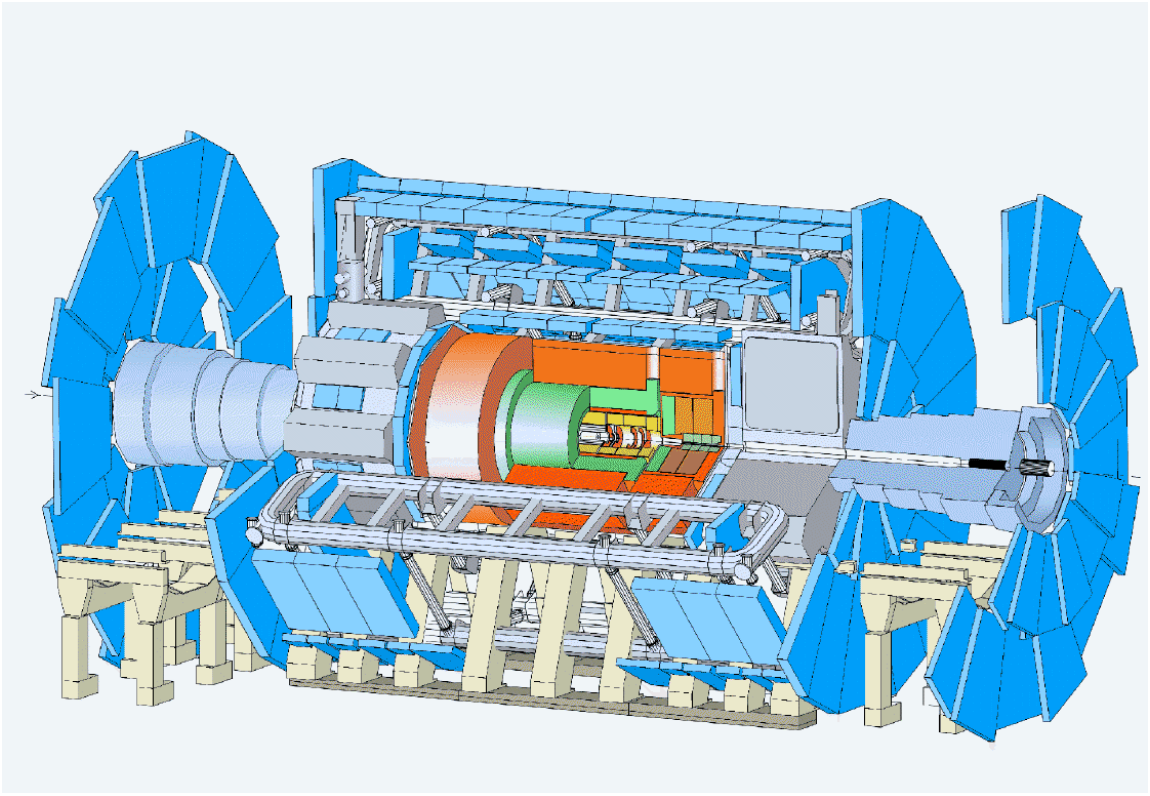

Figure 1-1 The ATLAS detector layout

- A tracker with semi-conductor pixel and strip detectors for very high accuracy measurements of the charged particle trajectories, followed by a straw-tube detector giving a bubble chamber like image of the event and independent electron identification. A thin superconducting solenoid coil provides a 2 T magnetic field for the tracker.
- A calorimeter with an inner cylinder in liquid-argon technology with its well-known high resolution, calibration precision and stability, followed at large radius by an iron-scintillator calorimeter providing good resolution in a very cost-effective manner.
- A high-precision stand-alone muon spectrometer, instrumented with detectors optimised for the requirements and environment at LHC, surrounding the calorimeter. A superconducting air-core toroidal magnet system provides the magnetic field for the muon spectrometer.

All systems have a large solid-angle coverage. In particular, precision measurements will be performed down to $\eta = 5$. The initial information flow from the ATLAS detectors is reduced by a dedicated selection system, the trigger, based on hierarchical decision-making. A data-acquisition system merges the information from the different systems and stores it for further processing and analysis. An object-oriented software system will reconstruct the stored detector signals, so as to access the physical properties of the produced particles. It will also simulate ATLAS in all relevant details.

The ATLAS detector concept was first presented in the Letter of Intent (LoI) [1] and latter in the Technical Proposal [2]. Since then the design has been developed much further, guided by detailed physics performance studies, experience from a rigorous and broad R&D programme, and the necessity to stay within cost-effective technologies which fulfil the essential physics requirements. Open options on some of the major detector components at the stage of the LoI and TP have been resolved, and some new ideas emerging from the significantly enlarged Collaboration have been implemented in the detector. ATLAS enters now in a new phase with most of the Technical Design Reports of all the components already submitted [3-7]. The construction phase is starting soon.

This paper is divided in 3 sections. Section 2 describes the ATLAS collaboration. The characteristics of the detector systems, including the DAQ/Trigger system are given in section 3. For details concerning the LHC physics prospects with the ATLAS detector see talk given by S. Gonzalez.

2 Human Resources

The ATLAS detector will be designed, constructed, and operated by a world-wide collaboration of scientists and engineers, forming 1700 members from 144 institutions and 33 countries. The age distribution of the ATLAS members is given in figure 2.1, with a mean age of 41 years. For ATLAS it is very important to keep a good fraction of the collaboration made of students that will ensure the running and expertise of the experiment over the next 20 years. Figures 2.2a and 2.2b show the distribution of CERN member and non-member states respectively within the ATLAS collaboration. 59% are from member states and 41% from non-member states.

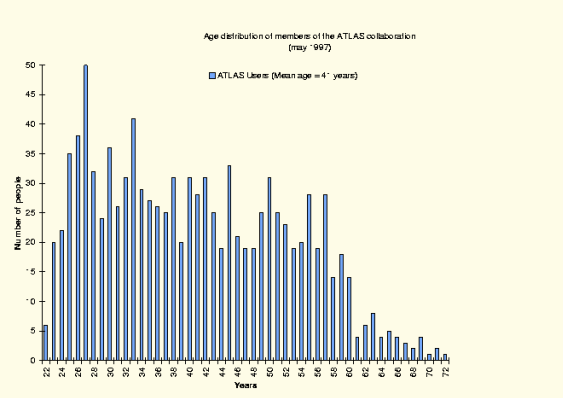

Figure 2-1 Age distribution of the ATLAS collaboration.

3 Detector layout

3.1 Magnet system

The ATLAS magnet system consists of 3 sub-systems [3]:

- A central Solenoid. It provides a central field of 2 T for the inner tracker
- The air-core Barrel Toroid and
- Two air cored End-Cap Toroids providing the field for the muon spectrometer.

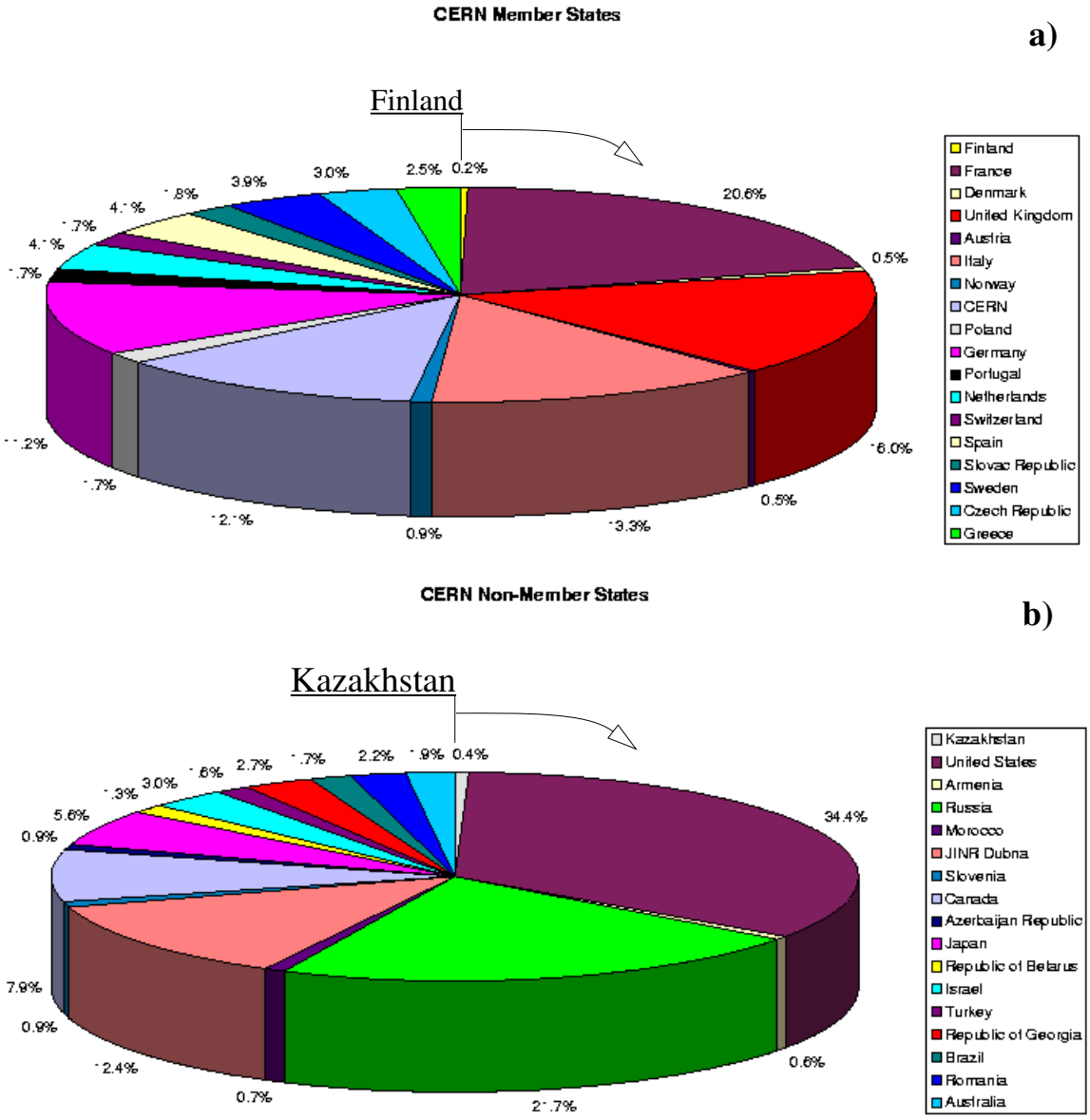

Figure 2-2 Distribution of ATLAS collaborators from CERN (a) member states, (b) non-member states.

A particular challenge of the ATLAS magnet system is its size and the hybrid configuration of solenoid and toroid coil systems while accommodating the physics requirements of a light and open structure.

Each of the three toroids consists of 8 coils assembled radially and symmetrically around the beam axis. The arrangement of the bare windings of all the coils in space is illustrated in figure 3.1. The toroid generates a stable, precise and predictable magnetic field in an enormous volume and is fully integrated with the detectors in an overall 20 x 20 x 25 m^3 assembly. In terms of magnetic field the central solenoid provides a central field of 2 T with a magnetic field peak of 2.6 T on the superconductor in the windings. The performance of the magnet system in terms of bending power is characterized by the field integral $\int Bdl$ where B is the azimuthal field component and dl is a straight line trajectory between the inner and outer

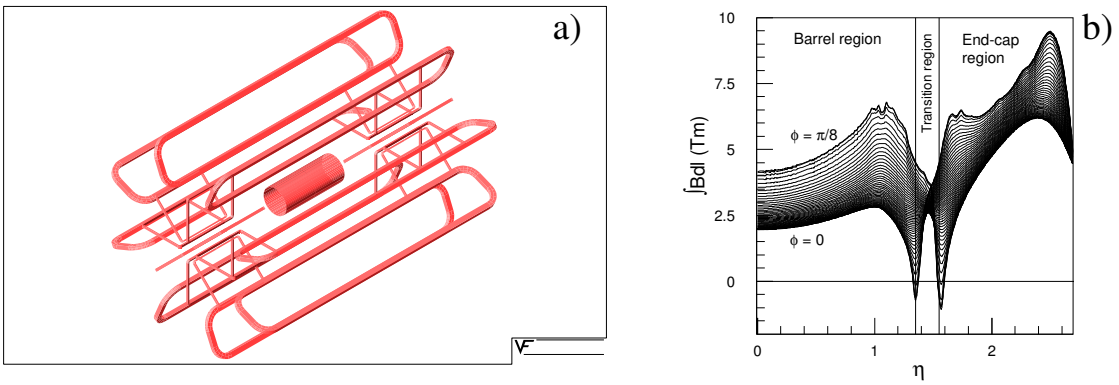

Figure 3-1 (a) Three dimensional view of the bare windings of the ATLAS magnet system: the central solenoid, the 8 coils of the Barrel Toroid and the 2x8 coils of the end-cap toroids. (b) Field integral versus pseudorapidity for various initial angles (iron of the Tile calorimeter and solenoid field are ignored).

radius of the toroids. The field as a function of the pseudorapidity for various initial angles is shown in figure 3.1b. The barrel toroid provides 2-6 Tm while the end-cap toroid contributes with 4-8 Tm in the 0.0-1.3 and 1.6-2.7 pseudorapidity ranges respectively. The magnetic field peaks on the superconductors in the barrel toroid and end-cap toroid are 3.9 and 4.1 T respectively.

3.2 Inner Detector

The task of the inner detector is to reconstruct the tracks and vertices in the event with high efficiency, contributing, together with the calorimeter and muon systems to the electron, photon and muon recognition, and supplying the important extra signature for short-lived particle decay vertices. Its acceptance covers the pseudo-rapidity region of $|\eta| < 2.5$, matching that of the rest of the ATLAS systems for precision measurements [4]. A three-dimensional cutaway view of the layout of the Inner Detector is shown in figure 3.2.

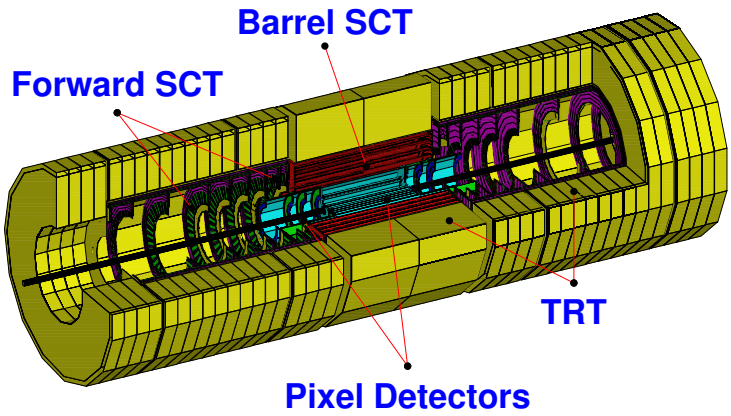

Figure 3-2 Three-dimensional cutway view of the ATLAS inner detector.

The momentum and vertex resolution targets require high-precision measurements to be made with fine-granularity detectors given the very large track density expected at the LHC. Semiconductor tracking (SCT) detectors, using silicon microstrip and pixel technology offer these features. Highest granularity around the vertex region is achieved using semiconductor pixel detectors. However, the total number of precision layers must be limited because of the material they introduce, and because of their high cost. At

Table 1. Parameters of the Inner Detector. The resolutions quoted are typical values (the actual resolution in each detector depends on |η|).

System	Position	Area (m^2)	Resolution σ (μm)	Channels (10^6)	η coverage
Pixels	1 removable barrel layer	0.2	$R\phi = 12$, $z = 66$	16	±2.5
	2 barrel layers	1.4	$R\phi = 12$, $z = 66$	81	±1.7
	4 end-cap disks on each side	0.7	$R\phi = 12$, $R = 77$	43	1.7-2.5
Silicon strips	4 barrel layers	34.4	$R\phi = 16$, $z = 580$	3.2	±1.4
	9 end-cap wheels on each side	26.7	$R\phi = 16$, $R = 580$	3.0	1.4–2.5
TRT	Axial barrel straws		170 (per straw)	0.1	±0.7
	Radial end-cap straws		170 (per straw)	0.32	0.7–2.5
	36 straws per track				

least four strip layers and three pixel layers are therefore crossed by each track in this design. A large number of tracking points (typically 36 per track) is given by a straw tube tracker (TRT) which provides the possibility of continuous track-following with much less material per point and at lower cost. The basic design parameters and the resolutions for space-point measurements are summarised in table 1.

The combination of the two techniques gives very robust pattern recognition and high precision in both φ and z coordinates. The straw hits at the outer radius contribute to the momentum measurement, with the lower precision per point compared to the silicon being compensated by the large number of measurements and the higher average radius. The relative precision of the different measurements are well matched, so that no single measurement dominates the momentum resolution. In addition, the electron identification capabilities of the whole experiment are enhanced by the detection of transition-radiation photons in the straw tubes.

The secondary vertex measurement performance will be enhanced with an innermost additional layer of pixels, at a radius of about 4 cm, as close as is practical around the beam pipe. A large amount of interesting physics can be done with this detector during the initial lower luminosity running, especially in the B sector, but recent physics studies have demonstrated the value of good b-tagging performance during all phases of the LHC, for example in Higgs and supersymmetry searches. The impact parameter resolution can be parametrised in Rφ as $\sigma(d_0) = 11 \oplus 60/p_T \sin\theta$ and in z as $\sigma(z_0) = 70 \oplus 100/p_T \sin^3\theta$ (in μm) with the dedicated B-physics layer present. The full simulation of this performance for different track transverse momenta is shown in figure 3.3 and 3.4.

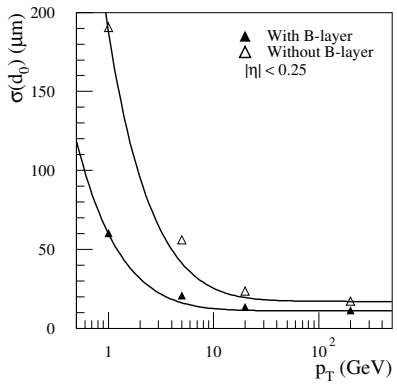

Figure 3-3 Transverse impact parameter resolution as a function of p_T for η=0.

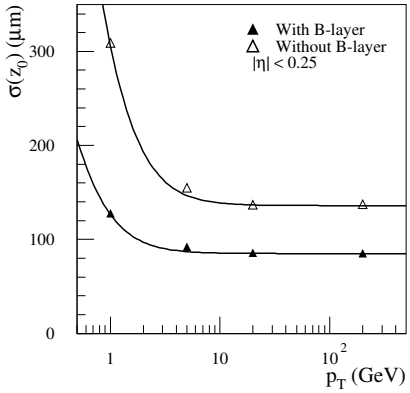

Figure 3-4 Longitudinal impact parameter resolution as a function of p_T for η=0.

The outer radius of the tracker cavity is 115 cm, fixed by the inner dimension of the cryostat containing the liquid argon EM calorimeter, and the total length is 7 m, limited by the position of the end-cap calorimetry. Mechanically, the Inner Detector consists of three units: a barrel part extending over 80 cm, and two identical end-caps covering the rest of the cylindrical cavity (see figure 3.2). In the barrel, the high-precision detector layers are arranged on concentric cylinders around the beam axis in the region with $|\eta| < 1$, while the end-cap detectors are mounted on disks perpendicular to the beam axis. More details on each subsystem of the inner detector are given below.

Pixel detector

The system consists of three barrels at average radii of ~ 4 cm, 11 cm, and 14 cm, and four disks on each side, between radii of 11 and 20 cm, which complete the angular coverage. The system is designed to be highly modular, containing approximately 1500 identical barrel modules and 1000 identical disk modules, and uses only one type of support structure in the barrel and one type in the disks.

The pixel modules are very similar in design for the disks and barrels. Each barrel module is 62.4 mm long and 22.4 mm wide, with 61440 pixel elements, read out by 16 chips each serving an array of 24 by 160 pixels. The output signals are routed on the sensor surface to a hybrid on top of the chips, and from there to a separate clock and control integrated circuit. The modules are overlapped on the support structure in order to give hermetic coverage. The thickness of each layer in the simulation is less than 1.39% of a radiation.

The chips must be radiation hard to withstand over 300 kGy of ionising radiation and over $5\ 10^{14}$ neutrons per cm^2 in ten years of operation. The system offers 140 million detector elements, each 50 mm in the Rϕ direction and 300 mm in z, which are invaluable for the task of pattern recognition in the crowded environment of the LHC.

SCT detector

The barrel SCT uses four layers of silicon microstrip detectors to provide precision points in the Rϕ and z coordinates, using small angle stereo to obtain the z measurement. Each silicon detector is 6.36×6.40 cm^2 with 768 read-out strips each with 80 mm pitch. The detector contains 61 m^2 of silicon detectors, with 6.2 million read-out channels. The spatial resolution is 16 mm in Rϕ and 580 mm in z. Tracks can be distinguished if separated by more than ~ 200 μm.

Solutions have been found to the critical issues in the system, and prototype modules have been successfully tested in beams in a magnetic field, showing the required performance in resolution, signal-to-noise and speed. Modules containing both front-end electronics and detectors, irradiated to the level expected for 10 years of LHC operation, have also been shown to function within specifications.

Transition Radiation Tracker

The TRT is based on the use of straw detectors, which can operate at the very high rates needed by virtue of their small diameter and the isolation of the sense wires within individual gas envelopes. Electron identification capability is added by employing xenon gas to detect transition-radiation photons created in a radiator between the straws.

Each straw is 4 mm in diameter, giving a fast response and good mechanical properties for a maximum straw length of 150 cm. The barrel contains about 50000 straws, each divided in two at the centre in order to reduce the occupancy and read out at each end. The end-caps contain 320000 radial straws, with the read-out at the outer radius. The total number of electronic channels is 420000. Each channel provides a drift-time measurement, giving a spatial resolution of 170 μm per straw, and two independent thresholds. These allow the detector to discriminate between tracking hits, which pass the lower threshold, and transition-radiation hits, which pass the higher.

A fast, low-noise preamplifier-shaper circuit with active baseline restoration has been developed to process the signals, using a radiation hard bipolar process. Position accuracies of about 170 µm have been achieved in tests at average straw counting rates of about 12 MHz. At these rates, only about 70% of the straws give correct drift time measurements because of shadowing effects, but the large number of straws per track guarantees a measurement accuracy of better than 50 µm averaged over all straws at the LHC design luminosity, including errors from alignment.

3.3 Calorimeter

Calorimeters will play a crucial role at the LHC, their intrinsic resolution improves with energy, which makes them very suitable detectors at high-energy machines. In particular, at the LHC, calorimeters will be the leading detectors in many measurements for the reconstruction of physics channels of prime interest. The tasks of the calorimeters at hadron colliders are: accurate measurement of the energy and position of electrons and photons; measurement of the energy and direction of jets, and of the missing transverse momentum of the event; particle identification, for instance separation of electrons and photons from hadrons and jets, and of t hadronic decays from jets; event selection at the trigger level [5]. In addition fast detector response (< 50 ns) and fine granular are required to minimise the impact of the pile-up on the physics performance. High radiation resistance is also needed, given the high particle fluxes expected over a period of operation of at least ten years.

The ATLAS calorimetry covers the range $|\eta|< 5$ using different techniques and devices as best suited for the different requirements and radiation environment. Table 2 shows the granularity of the different calorimeter components in the full η range. A view of the ATLAS calorimetry is presented in figure 3.5. It consists of an electromagnetic calorimeter covering the rapidity region $|\eta|< 3.2$, barrel hadronic calorimeter covering $|\eta|< 1.7$, hadronic end-cap calorimeters covering $1.5 <|\eta|< 3.2$, and forward calorimeters covering $3.1 <|\eta|< 4.9$. The radius of the inner-detector cavity is 1.15 m and its half-length 3.45 m. The LAr calorimeter system is contained in a cylinder of outer radius 2.25 m and total length spanning 6.65m along the beam axis. The Tile calorimeter system has an outer radius of 4.23 m and a total length spanning 6.10m. The total weight of the calorimeter system is about 4 000 tons.

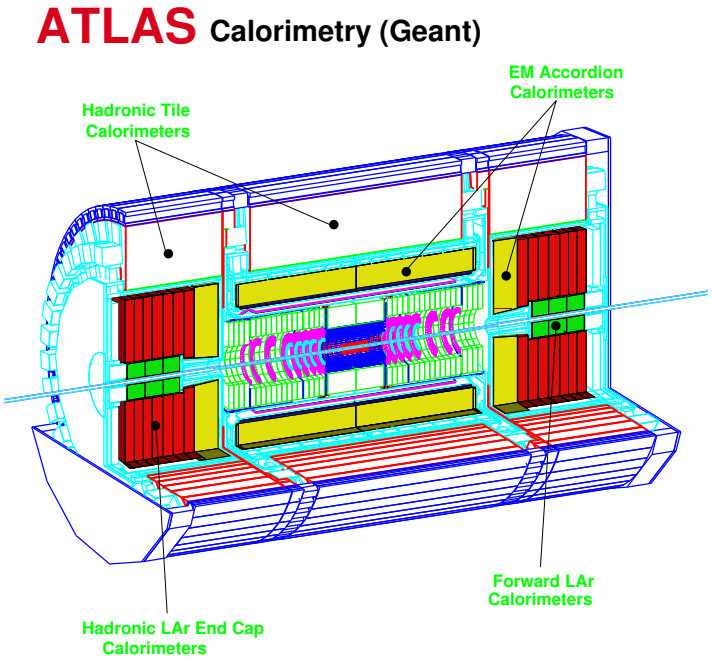

Figure 3-5 View of the ATLAS calorimetry.

The electromagnetic calorimeter

The EM calorimeter is a lead–Liquid-Argon (LAr) detector with accordion geometry [6], see figure 3.6. In the pseudorapidity range $|\eta|< 1.8$ it is preceded by a presampler detector, installed immediately behind the cryostat cold wall, and used to correct for the energy lost in the material (inner detector, cryostats, coil) upstream of the calorimeter. The lead absorber thickness is chosen such that the thickness is above 24 X_0 in the barrel and $26X_0$ in the end-caps. The rapidity coverage, granularity and longitudinal segmentation of the ATLAS calorimetry are summarised in Table 2. The total number of channels is about 200000.

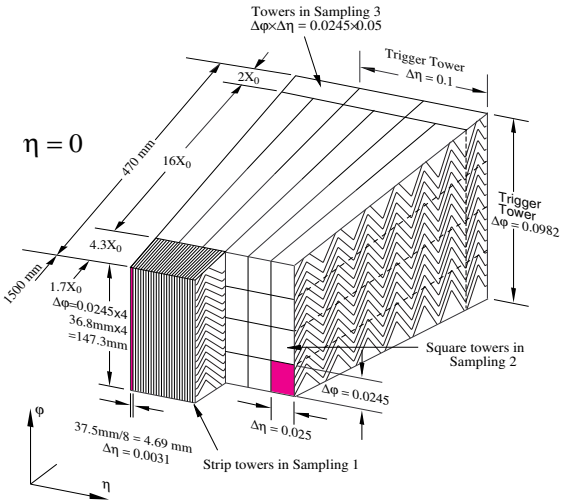

Figure 3-6 Sketch of the accordion structure of the electromagnetic calorimeter.

The measured electron energy resolution is shown in figure 3.7 for various η values. This result gives a sampling term of (9.90-10.4)%, a local constant term of (0.27-0.35)% and a noise term of (280-520) MeV over this η range. As opposed to the other terms, which are mostly a reflection of the design, the constant term is more sensitive to the skill put into the construction, calibration, and operation of the detector.

This accuracy is needed to achieve a mass resolution of ~1% for the $H \rightarrow \gamma\gamma$ and $H \rightarrow 4e$ channels in the mass region 90–180 GeV. To avoid worsening the sampling term at low energy, a presampler has been added where necessary, in order to correct for energy losses in the dead material upstream (tracker, coil, cryostat, etc.).

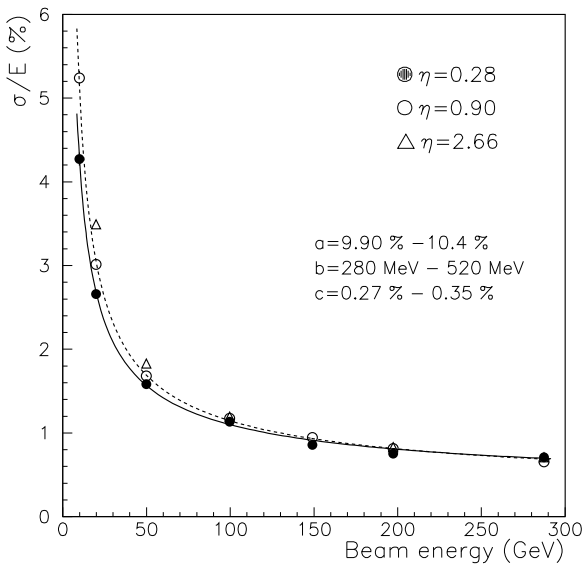

Figure 3-7 Measured electron energy resolution at various η values.

Beyond energy measurement, the EM calorimeter will provide, thanks to its high granularity, powerful electron/photon identification and rejection of the jet background. The thin strips in the first sampling are a unique feature of this calorimeter. They allow π^0 rejection, by a factor larger than 3 at 50 GeV ET. In total, the jet rejection, at 20 GeV or above, is expected to be about 5000. Such a rejection is required to eliminate huge QCD backgrounds in the H-->γγ channel. The narrow strips contribute also to the photon angular measurement in the η direction, with an accuracy of about 50 mrad/$\sqrt{E(GeV)}$, an essential information in the reconstruction of the channel mentioned above.The calorimeter is also an essential tool in identifying τ decays into hadrons. Combined with the tracker, a rejection of about 400 against jets is possible for about 30% efficiency, allowing to improve in an essential way the signal to background ratio in the search for MSSM Higgs bosons (A/H) decaying into ττ.

Table 2. Rapidity coverage, granularity and longitudinal segmentation of the ATLAS calorimeters.

EM CALORIMETER	**Barrel**	**End-cap**	
Coverage	$\|\eta\| < 1.475$	$1.375 < \|\eta\| < 3.2$	
Longitudinal segmentation	3 samplings	3 samplings 2 samplings	$1.5 < \|\eta\| < 2.5$ $1.375 < \|\eta\| < 1.5$ $2.5 < \|\eta\| < 3.2$
Granularity ($\Delta\eta \times \Delta\phi$) Sampling 1	0.003×0.1	0.025×0.1 0.003×0.1 0.004×0.1 0.006×0.1 0.1×0.1	$1.375 < \|\eta\| < 1.5$ $1.5 < \|\eta\| < 1.8$ $1.8 < \|\eta\| < 2.0$ $2.0 < \|\eta\| < 2.5$ $2.5 < \|\eta\| < 3.2$
Sampling 2	0.025×0.025	0.025×0.025 0.1×0.1	$1.375 < \|\eta\| < 2.5$ $2.5 < \|\eta\| < 3.2$
Sampling 3	0.05×0.025	0.05×0.025	$1.5 < \|\eta\| < 2.5$
PRESAMPLER	**Barrel**	**End-cap**	
Coverage	$\|\eta\| < 1.52$	$1.5 < \|\eta\| < 1.8$	
Longitudinal segmentation	1 sampling	1 sampling	
Granularity ($\Delta\eta \times \Delta\phi$)	0.025×0.1	0.025×0.1	
HADRONIC TILE	**Barrel**	**Extended barrel**	
Coverage	$\|\eta\| < 1.0$	$0.8 < \|\eta\| < 1.7$	
Longitudinal segmentation	3 samplings	3 samplings	
Granularity ($\Delta\eta \times \Delta\phi$) Samplings 1 and 2 Sampling 3	 0.1×0.1 0.2×0.1	 0.1×0.1 0.2×0.1	
HADRONIC LAr		**End-cap**	
Coverage		$1.5 < \|\eta\| < 3.2$	
Longitudinal segmentation		3 samplings	
Granularity ($\Delta\eta \times \Delta\phi$)		0.1×0.1 0.2×0.2	$1.5 < \|\eta\| < 2.5$ $2.5 < \|\eta\| < 3.2$
FORWARD CALORIMETER		**End-cap**	
Coverage		$3.1 < \| \eta \| < 4.9$	
Longitudinal segmentation		3 samplings	
Granularity ($\Delta\eta \times \Delta\phi$)		$\sim 0.2 \times 0.2$	

The Tile hadronic calorimeter

In the range $|\eta| < 1.6$ the iron-scintillating-tiles technique is used for the barrel and extended barrel Tile calorimeters and for partially instrumenting the crack between them with the Intermediate Tile calorimeter (ITC) [7]. This gap provides space for cables and services from the innermost detectors. The hadronic barrel calorimeter is a cylinder with an inner radius of 2.28 m to an outer radius of 4.23 m. It is divided in three sections: the central barrel and two extended barrels. It is based on a sampling technique with plastic scintillator plates (tiles) embedded in an iron absorber and read out by wave length shifting fibres. The tiles are placed in plane perpendicular to the beam axis and staggered in depth, simplifying the mechanical construction and the fibre routing, see figure 3.8.

It is segmented in three layers, approximately 1.4, 4.0 and 1.8 λ thick at η = 0. Azimuthally, the barrel and extended barrels are divided into 64 modules. In η, the read-out cells, built by grouping fibres into a photomultiplier, are pseudo-projective to the interaction region. The resulting granularity of the Tile calorimeter is given in table 2. The total number of channels is of the order of 10 000. The calorimeter is placed behind the EM calorimeter (~1.2 λ) and the solenoid coil. So the total active calorimeter thickness (EM + Tile) is 9.2 λ at η=0. The amount of material in front of the muon system, that includes the support structure of the Tile calorimeter, is 11 λ at η=0.

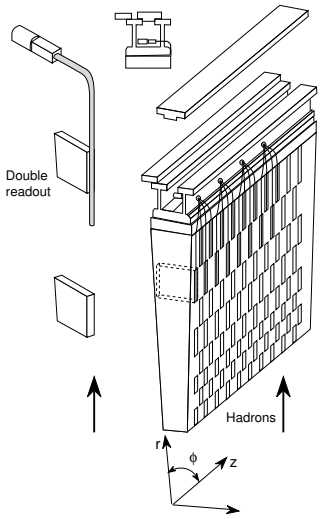

Figure 3-8 The principle of the Tile Calorimeter design.

For the hadronic calorimeter the guidelines for the energy resolution performances are set requiring a jet energy resolution at different levels in different η regions:

$$\frac{\Delta E}{E} = \frac{50\%}{\sqrt{E}} \oplus 3\% \text{ for } |\eta| < 3 \text{ and } \frac{\Delta E_T}{E_T} = \frac{100\%}{\sqrt{E}} \oplus 10\% \text{ for } 3 < |\eta| < 5.$$

Such resolutions are adequate to the tasks of providing jet reconstruction and jet-jet mass reconstruction as well as missing p_T measurement for physical process of interest. Figure 3.9 shows the measured pion energy resolution obtained with the Tile calorimeter tested in standalone mode and with the combined set-up of the two calorimeters: electromagnetic LAr and hadronic Tile barrel calorimeters. A fit to the experimental points for the combined setup, after weigthing give:

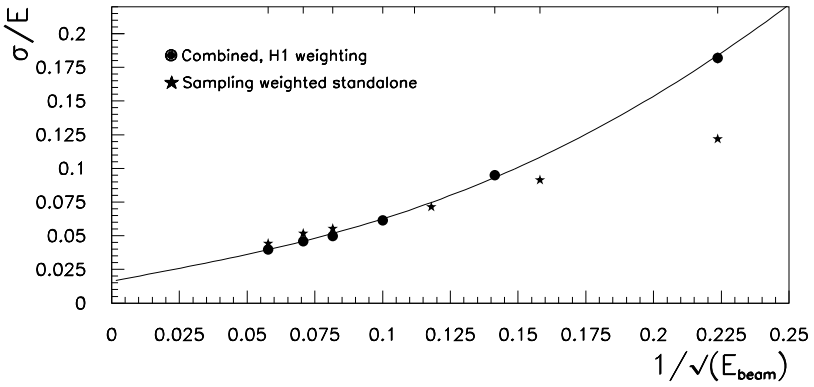

Figure 3-9 Measured pion energy resolution obtained with the combined setup of the two calorimeters: electromagnetic LAr and hadronic Tile barrel calorimeters and with the Tile calorimeter tested in standalone mode. Weighting algorithms have been used.

$$\left(\frac{(38.3 \pm 4.6)}{\sqrt{E}}\% + (1.62 \pm 0.29)\%\right) \oplus \frac{(3.06 \pm 0.18)}{E} \quad \text{(E in GeV)}$$

The LAr hadronic calorimeters

In the range ~1.5 <|η|< 4.9 the Liquid Argon calorimetry takes over: the end-cap hadronic calorimeter extends till |η|< 3.2 while the range 3.1 <|η|< 4.9 is covered by the high-density forward calorimeter. Both the hadronic end-cap and the forward calorimeters are integrated in the same cryostat housing also the EM end-caps. Each hadronic end-cap calorimeter consists of two, equal diameter, independent wheels.

The first wheel is built out of 25 mm copper plates, while the second one uses 50 mm plates; in both wheels the gap between consecutive copper plates is 8.5 mm, and is equipped with 3 electrodes that split it in 4 drift spaces of ~1.8 mm each. The first wheel is divided in two longitudinal read-out segments (of respectively 8 and 16 layers in depth), while the second wheel has only one segment, of 16 layers. The read-out cells are fully pointing in ϕ but only "pseudo pointing" in η. The thickness of the active part of the end-cap calorimeter is ~12 λ.

In ATLAS the forward calorimeter is integrated in the end-cap cryostat, with the front face at about 5 meters from the interaction point. This makes the forward calorimeter a particularly challenging detector due to the high level of radiation, however providing a clear benefit in terms of uniformity of coverage, reducing to the minimal possible level the effects of the crack and dead space in the transition region around $\eta = 3.1$, with advantages for the efficiency of forward jet tagging and for the reduction of the tails in the distribution. The forward calorimeter has to accommodate at least 9 interaction lengths of active detector in a rather short longitudinal space, and thus it is a high density detector, consisting of three longitudinal sections: the first one is in copper, while the other two are tungsten. In each of them the calorimeter consists of a metal matrix with regularly spaced longitudinal channels filled with rods. The sensitive medium is Liquid Argon and fills the gap between the rod and matrix: the gaps are 250 microns wide in the first section and 375 (500) microns in the second (last) one. In the forward calorimeter the electronic noise in a jet cone of $\Delta R=0.5$ is ~1 GeV ET at $\eta = 3.2$ and drops quickly to 0.1 GeV in ET at $\eta = 4.6$.

3.4 Muon spectrometer

High-momentum final-state muons are amongst the most promising and robust signatures of physics at the Large Hadron Collider (LHC). The discovery potential of the spectrometer has been optimised on the basis of selected benchmark processes, in particular Standard Model and supersymmetric Higgs decays and new vector bosons. To obtain a good performance of the apparatus for transverse momenta which are small on the scale of LHC physics, beauty physics and CP violation have also been studied. Important parameters that need to be optimised for maximum physics reach are: resolution, second-coordinate measurement, rapidity coverage of track reconstruction, trigger selectivity, trigger coverage and bunch-crossing identification. To exploit this potential, the ATLAS collaboration has designed a high-resolution muon spectrometer with stand-alone triggering and momentum measurement capability over a wide range of transverse momentum, pseudorapidity, and azimuthal angle [8]. The view of the muon spectrometer is shown in figure 3.10.

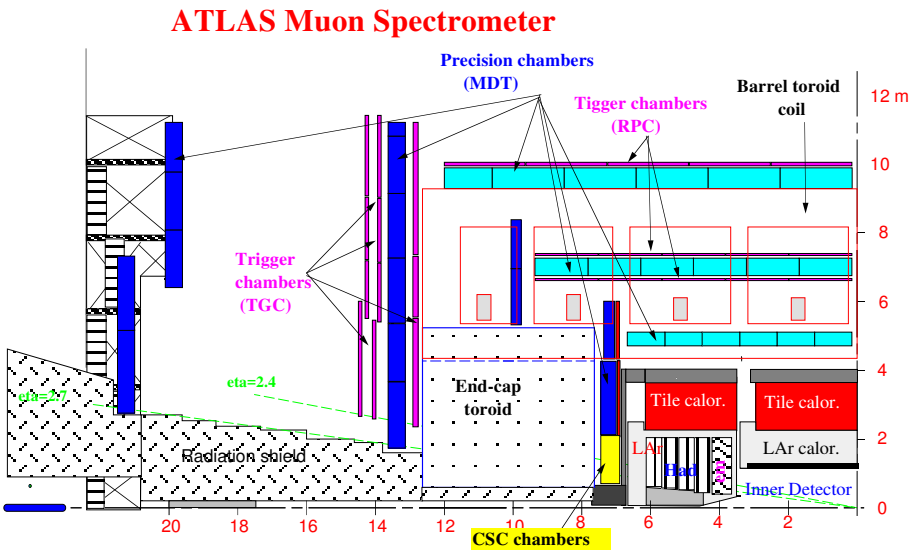

Figure 3-10 Longitudinal view of the muon spectrometer.

The muon spectrometer is based on the magnetic deflection of muon tracks in a system of three large superconducting air-core toroid magnets instrumented with separate-function trigger and high-precision tracking chambers. In the pseudorapidity range $|\eta| < 1.0$, magnetic bending is provided by a large barrel magnet constructed from eight coils surrounding the hadron calorimeter (see section 3.1). For $1.4 < |\eta| < 2.7$, muon tracks are bent in two smaller end-cap magnets inserted into both ends of the barrel toroid. In the interval $1.0 < |\eta| < 1.4$ referred to as transition region, magnetic deflection is provided by a combination of barrel and end-cap fields. This magnet configuration provides a field that is mostly orthogonal to the muon trajectories, while minimizing the degradation of resolution due to multiple scattering.

The design and performance of the muon spectrometer must satisfy exacting, and sometimes conflicting, requirements of three different kinds:

- the largest possible discovery reach for expected and unexpected new physics, with minimal systematic biases;
- good discrimination against high levels of charged and neutral particle background from minimum-bias events and radiation;
- safe and reliable operation in difficult environmental conditions for the anticipated lifetime of the LHC.

The momentum resolution of the spectrometer is limited by intrinsic detector resolution, chamber calibration errors, chamber positioning uncertainties, multiple scattering, and statistical fluctuations of energy loss in the calorimeter. The different contributions to the barrel momentum resolution are shown in figure 3.11a; a similar picture is obtained for the end-caps.

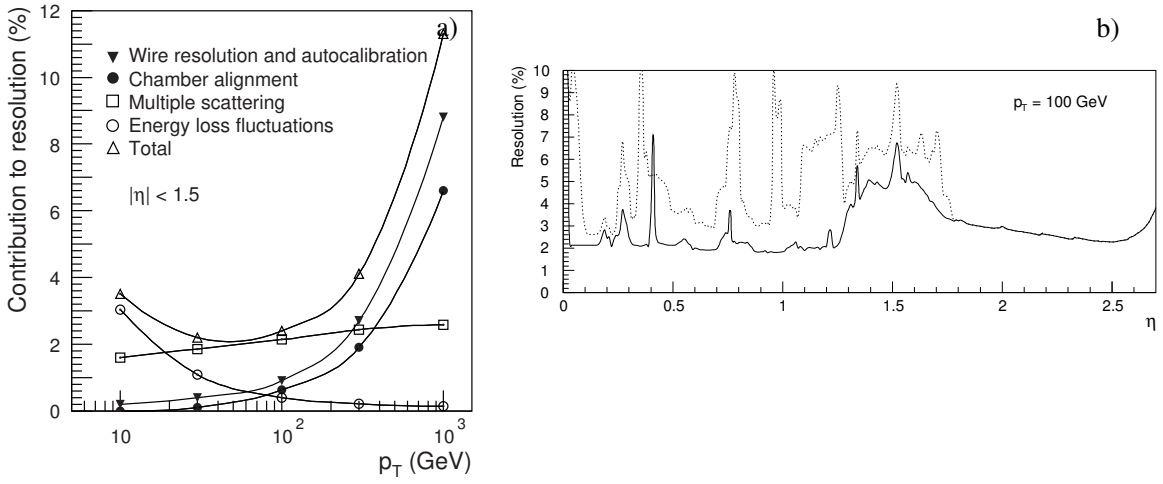

Figure 3-11 (a) Contributions to the momentum resolution of the muon spectrometer, averaged over $|\eta| < 1.5$ and azimuthal angle, in a standard sector. (b) Momentum resolution for p_T = 100 GeV as a function of η averaged over all azimuth angles. The solid curve applies to a standard sector; the dotted curve corresponds to one of the bottom sectors, where barrel toroid coils are captured inside the support structure for the inner parts of the detector.

The behaviour observed is typical for open-geometry magnetic spectrometer. The resolution is limited by energy loss fluctuations at small momenta and by detector resolution at high momenta, whereas the multiple scattering effect is approximately momentum-independent. The momentum resolution is typically 2–3% over most of the kinematic range apart from very high momenta, where it increases to ~ 10% at p_T = 1 TeV. The momentum resolution is shown in figure 3.11b as a function of pseudorapidity for p_T = 100 GeV muons. The resolution is largely con-

stant over the η range of the spectrometer, with the exception of some spikes at pseudorapidities obstructed by barrel magnet elements, and of an enhancement around $\eta = 1.5$ owing to a degraded bending power in the transition region between barrel and end-cap magnets. < 1.5.

Monitored Drift Tubes

Over most of the pseudorapidity range, a precision measurement of the track coordinates in the principal bending direction of the magnetic field is provided by Monitored Drift Tubes (MDTs). The basic detection elements are aluminium tubes of 30 mm diameter and 400 μm wall thickness, with a 50 μm diameter central W–Re wire. The tubes are operated with a non-flammable Ar-CH_4-N_2 mixture at 3 bar absolute pressure. The envisaged working point provides for a highly linear space–time relation with a maximum drift time of ~ 500 ns, a small Lorentz angle, and good ageing properties due to small gas amplification. The single-wire resolution is typically 80 μm. To improve the resolution of a chamber beyond the single-wire limit and to achieve adequate redundancy for pattern recognition, the MDT chambers are constructed from 2×4 monolayers of drift tubes for the inner and 2×3 monolayers for the middle and outer stations. The tubes are arranged in multilayers of three or four monolayers, respectively, on either side of a rigid support structure. The construction of prototypes has demonstrated that they can be built to the required mechanical accuracy of ~ 30 μ m.
Table 3 summarizes the number of chambers, the area covered, and the number of read-out channels for the four chamber technologies.

Table 3. Overview of the muon chamber instrumentation. 'Area covered' refers to chamber modules which normally contain several detector layers.

	Precision chambers		Trigger chambers	
	CSC	**MDT**	**RPC**	**TGC**
Number of chambers	32	1194	596	192
Number of readout channels	67 000	370 000	355 000	440 000
Area covered (m^2)	27	5500	3650	2900

Cathode Strip Chambers

In the first station in the end-cap region and for pseudorapidities $|\eta| > 2$, Cathode Strip Chambers (CSCs) are used to provide a finer granularity which is required to cope with the demanding rate and background conditions in this region of the apparatus.
The CSCs are multiwire proportional chambers with cathode strip read-out and with a symmetric cell in which the anode-cathode spacing is equal to the anode wire pitch. The precision coordinate is obtained by measuring the charge induced on the segmented cathode by the avalanche formed on the anode wire. Good spatial resolution is achieved by segmentation of the read-out cathode and by charge interpolation between neighbouring strips. The cathode strips for the precision measurement are oriented orthogonal to the anode wires. The anode wire pitch is 2.54 mm and the cathode read-out pitch is 5.08 mm; r.m.s. resolutions of better than 60 μm have been measured in several prototypes. Other important characteristics are small electron drift times (30 ns), good time resolution (7 ns), good two-track resolution, and low neutron sensitivity. A measurement of the transverse coordinate is obtained from orthogonal strips, i.e. oriented parallel to the anode wires,
The CSCs are arranged in 2×4 layers. The design utilizes low-mass construction materials to minimize multiple scattering and detector weight. The present baseline CSC gas is a non-flammable mixture of 30% Ar, 50% CO_2 and 20% CF_4, with a total volume of about 1.1 m^3. The fact that this gas contains no hydrogen, combined with the small gap width, explains the low sensitivity to neutron background. In general, the CSC performance is less sensitive to variations of the gas parameters than that of the MDTs.

Trigger chambers (RPCs and TGCs)

The trigger chambers for the ATLAS muon spectrometer serve a threefold purpose, and must therefore fulfil the following basic requirements:

- bunch crossing identification, requiring a time resolution better than the LHC bunch spacing of 25 ns;
- a trigger with well-defined p_T cut-off in moderate magnetic fields, requiring a granularity of the order of 1 cm;
- measurement of the second coordinate in a direction orthogonal to the one measured in the precision chambers with a typical resolution of 5–10 mm.

The proposed system employs two different types of detectors, Resistive Plate Chambers (RPCs) in the barrel ($|\eta| < 2.4$) and Thin Gap Chambers (TGCs) in the end-cap region. Both types of trigger chambers also provide a 'second-coordinate' measurement of track coordinates orthogonal to the precision measurement, in a direction approximately parallel to the magnetic field lines. The second-coordinate capability of the trigger chambers is designed to match the acceptance of the precision chambers.

The trigger chambers cover a total area of about 3650 m^2 in the barrel and 2900 m^2 in the end-cap region, each chamber containing at least two detector layers. The total number of channels is about 350 000 for the barrel and 440 000 in the end-caps, see table 3.

The RPC is a gaseous detector providing a typical space–time resolution of 1 cm × 1 ns with digital read-out. The basic RPC unit is a narrow gas gap formed by two parallel resistive bakelite plates, separated by insulating spacers. The primary ionization electrons are multiplied into avalanches by a high, uniform electric field of typically 4.5 kV/mm. Amplification in avalanche mode produces pulses of typically 0.5 pC. The candidate gas mixture is based on tetrafluoroethane ($C_2H_2F_4$), a non-flammable and environmentally safe gas that allows for a relatively low operating voltage. The signal is read out via capacitive coupling by metal strips on both sides of the detector. A trigger chamber is made from two rectangular detector layers, each one read out by two orthogonal series of pick-up strips: the 'η strips' are parallel to the MDT wires and provide the bending view of the trigger detector; the 'ϕ strips', orthogonal to the MDT wires, provide the second-coordinate measurement which is also required for the offline pattern recognition.

The TGC chambers are designed in a way similar to multiwire proportional chambers, with the difference that the anode wire pitch is larger than the cathode–anode distance. Signals from the anode wires, arranged parallel to the MDT wires, provide the trigger information together with read-out strips arranged orthogonal to the wires. The read-out strips also serve to measure the second coordinate. Using a highly quenching gas mixture of 55% CO_2 and 45% *n*-pentane (*n*-C_5H_{12}), this type of cell geometry permits operation in saturated mode. The main dimensional characteristics of the chambers are a cathode-cathode distance (gas gap) of 2.8 mm, a wire pitch of 1.8 mm, and a wire diameter of 50 μm. The operating high voltage foreseen is 3.1 kV. The electric field configuration and the small wire distance provide for a short drift time and thus a good time resolution. As the angle increases, the tracks pass closer to the wire, thus reducing the maximum drift distance and improving the time resolution. In the ATLAS chamber layout, all muons passing through TGCs with transverse momenta above the required threshold have incident angles greater than ~ 10°.

3.5 Trigger and DAQ

The ATLAS trigger is organized in three trigger levels (LVL1, LVL2, LVL3), as shown in figure 3.12 [2]. At LVL1, special-purpose processors act on reduced-granularity data from a subset of the detectors. The LVL2 trigger uses full-granularity, full-precision data from most of the detectors, but examines only regions of the detector identified by LVL1 as containing interesting information. At LVL3, the full event data are used to make the final selection of events to be recorded for offline analysis.The LVL1 trigger accepts data at the full LHC bunch-crossing rate of 40 MHz (every 25 ns). The latency (time taken to form and distribute the LVL1 trigger decision) is about 2 μs, and the maximum output rate is limited to 100 kHz by the capabilities of the subdetector read-out systems and the LVL2 trigger. During the LVL1 processing, the data from all parts of the ATLAS detector are held in pipeline memories. Requirements on the LVL1 trigger are that it must identify unambiguously the bunch crossing containing the interaction of interest and introduce negligible dead time.

The LVL2 trigger reduces the rate from up to 100 kHz after LVL1 to about 1 kHz. The information from the LVL1 trigger system is used to identify the regions of the detector containing interesting features such as high p_T electromagnetic clusters (electrons or photons), jets and muons. The LVL2 trigger then has to access and process only a small fraction of the total detector data, with corresponding advantages in terms of the required processing power and data-movement capacity. The total LVL2 latency is variable, up to about 10 ms. After an event is accepted by the LVL2 trigger, the full data are sent to the LVL3 processors via the event builder (EB). Complete event reconstruction is possible at LVL3, with decision times up to about 1 s.

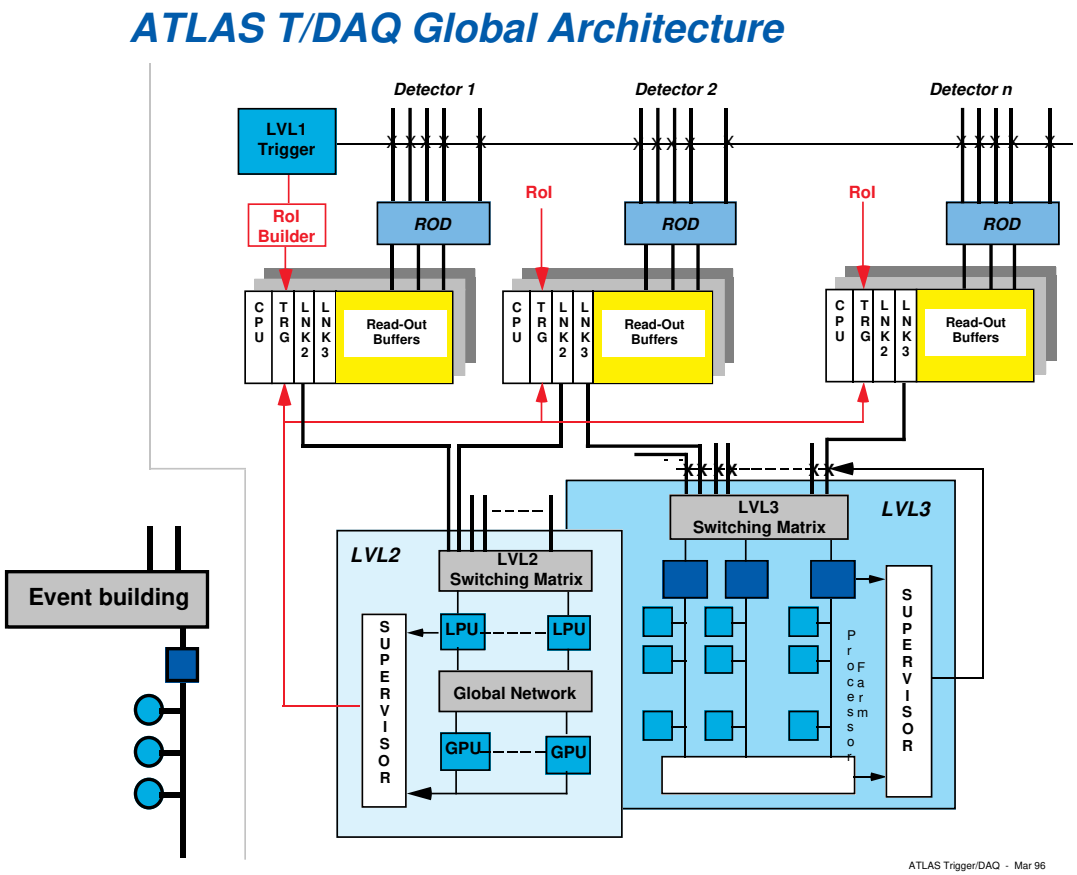

Figure 3-12 The ATLAS trigger and DAQ architecture.

The LVL3 system must achieve a data-storage rate of 10--100 MB/s by reducing the event rate and/or the event size. For some triggers, for example Higgs boson candidates, the full event data will be recorded with an event size of about 1 MB, corresponding to a maximum event rate of about 100 Hz. Only muon and calorimeter information is used in separate LVL1 processors to evaluate various trigger conditions. Inner detector information is not used at LVL1 because of the complexity of the events at high luminosity and because the rates can be reduced to acceptable levels without it. Full-precision information from the inner detector, as well as from the calorimeter and muon detectors is however used at LVL2. For example, sufficiently complicated processing is foreseen to find tracks and measure their p_T. This is particularly important in the case of the electron trigger, where the LVL1 rate is dominated by background from jets with a large e.m. content. Particular features will be exploited for the B-physics selection, initiated at LVL1 with a low p_T inclusive-muon trigger. As an example, the electron identification capability of the TRT is used at LVL2 to select J/ψ-->e^+e^- decays with electron p_T down to 1 GeV. At LVL3, the full event information will be available, making possible the use of complex signatures such as displaced secondary vertices and K^o_s decays.

Algorithms that will be used at LVL1 and LVL2, rates and efficiencies for signals and backgrounds have been evaluated with detailed physics and detector Monte Carlo simulations. It is to be noted that the trigger processors at all three levels will be programmable, so that the trigger criteria can be adapted according to the experience from initial running, and to increasing luminosity of LHC.

The full data of each event accepted by LVL2 are assembled and transferred to a farm of processors that perform full-event analysis and make the LVL3 selection before permanent recording. The data-merging stage will be based on a high-speed switching network, interconnecting Data Acquisition (DAQ) memories and LVL3 processing units, supervised by data-flow manager components. It is too early at this stage to freeze the technological implementation of the DAQ system. The architecture of technology-independent implementations of DAQ models is being investigated with detailed system performance simulations using front-line software tools.

Preprototype hardware for the LVL1 and LVL2 trigger processors and clock distribution system has been developed. The processors have been successfully tested in connection with subdetector test beam data-taking. Trigger and DAQ prototyping and testing is an integral part of the test beam activities with complete prototype detector systems of ATLAS.

References

[1] ATLAS Letter of Intent for a General-Purpose pp Experiment at the Large Hadron Collider at CERN, CERN/LHCC/92--4, LHCC/I2 (1992).

[2] The ATLAS Technical Proposal for a General Purpose pp Experiment at the Large Hadron Collider at CERN, CERN/LHCC/94–43 (1994).

[3] ATLAS Magnet System Technical Design Reports, CERN/LHCC 97-18/19/20 (1997).

[4] ATLAS Inner Detector Technical Design Reports, CERN/LHCC 97-16/17 (1997).

[5] ATLAS Calorimeter Performance Technical Design Report, CERN/LHCC/96-40 (1996).

[6] ATLAS Liquid Argon Calorimeter Technical Design Report, CERN/LHCC 96-41 (1996).

[7] ATLAS Tile Calorimeter Technical Design Report, CERN/LHCC 96-42 (1996).

[8] ATLAS Muon SpectrometerTechnical Design Report, CERN/LHCC 97-22 (1997).

[9] ATLAS Computing Technical Proposal, CERN/LHCC/96-43 (1996).